Task 1.2

Title

Reservoir stimulation and engineering

Projects (presented on the following pages)

A true triaxial frame for hydraulic stimulation
Thomas Blum, Dmitry Loginov, Brice Lecampion

Fluid induced aseismic slip in a Discrete Fracture Network: marginally pressurized vs critically stressed case
Federico Ciardo, Brice Lecampion

Effect of dilatancy on the transition from aseismic to seismic slip due to fluid injection in a fault
Federico Ciardo, Brice Lecampion

Critically-stressed reservoir stimulation direction via stress preconditioning
Barnaby Fryer, Xiaodong Ma, Gunter Siddiqi, Lyesse Laloui

Geomechanical response of carbonate-rich Opalinus clay to CO_2
Taeheon Kim, Alberto Minardi, Lyesse Laloui

On the seismo-hydro-mechanical response of a shear zone during hydraulic stimulation
H. Krietsch, L. Villiger, J. Doetsch, V. Gischig, M. R. Jalali, F. Amann

Laboratory hydraulic fracturing tests in low-permeability rocks
D. Liu, T. Blum, B. Lecampion

Fluid injection driven, a-seismic fracture growth with remote nucleation on heterogeneous fault
Andreas Möri, Brice Lecampion, Federico Ciardo

Hydraulic fracture in transversely isotropic material: propagation perpendicular to the isotropy plane
Fatima-Ezzahra Moukhtari, Brice Lecampion

A fast 3D BEM solver for fracture mechanics
Carlo Peruzzo, Elizaveta Gordeliy, Dmitry Nikolskiy, Brice Lecampion, François Fayard

Added value of smart storage operations on an alpine run-off-river HPP obtain from hydrological-hydraulic modelling
Maria Ponce, Jessica Zordan, Pedro Manso, Cécile Münch

PyFrac – A planar 3D solver for hydraulic fracture growth
Haseeb Zia, Brice Lecampion

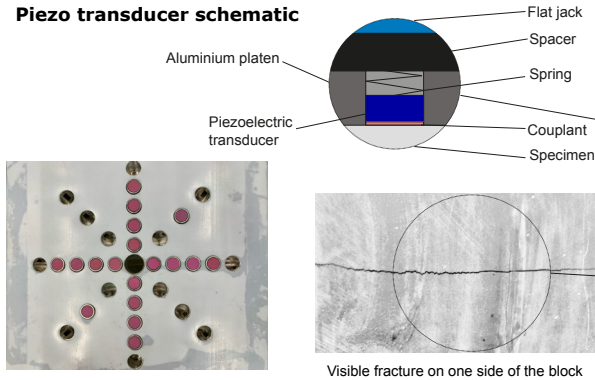# A true triaxial frame for hydraulic stimulation

Thomas Blum, Dmitry Loginov, Brice Lecampion
Geo-Energy Laboratory - Gaznat chair on Geo-energy, EPFL, Lausanne, Switzerland

Elastic wave monitoring system

- 64 piezoelectric transducers arranged in 32 sources and 32 receivers (800 kHz)
- Both longitudinal and shear transducers in order to use both P- and S-waves
- Sequential excitation of all 32 sources up to every few seconds for snapshots of the mechanical properties during fracture propagation, using the following arrivals:

  R – reflected signal → fluid content of the fracture
  D – diffracted signal → position of the fracture tip
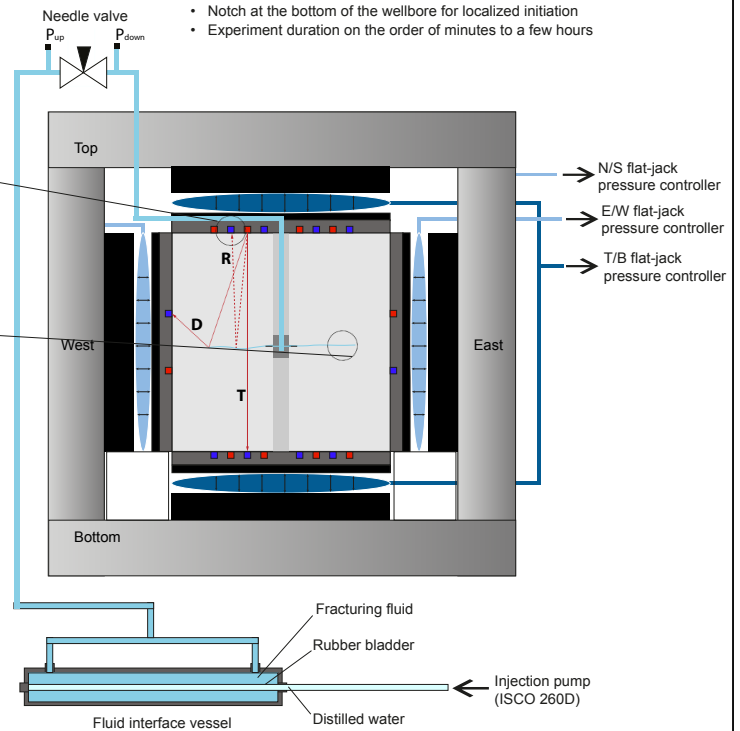 T – transmitted signal fracture thickness

Piezo transducer schematic

Flat jack
Spacer
Spring
Aluminium platen
Piezoelectric transducer
Couplant
Specimen

Piezo transducers array

Visible fracture on one side of the block

Top-view photo inside the reaction frame, with flat-jacks and platen on the sides of the specimen, and platen with piezo transducers on top.
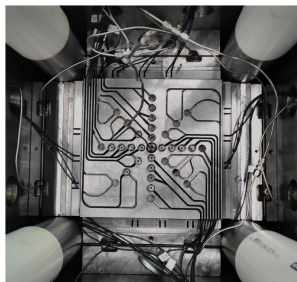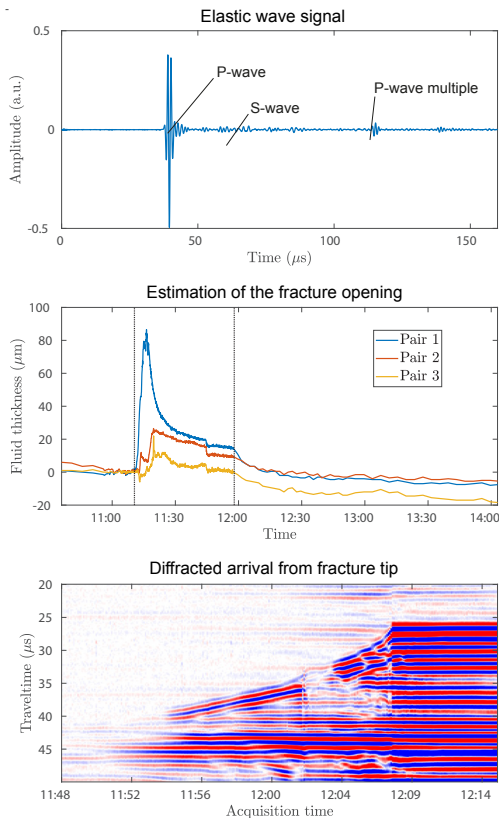
Experimental setup characteristics

- Cubic geologic specimen, 250 x 250 x 250 mm
- Reaction frame: confining stresses of up to 25 MPa along each axis
- Independently controlled pairs of flat-jacks to apply confining stresses
- High-pressure injection pump: flow rate from 1 μL/s to 100 mL/s
- 51 MPa maximum injection pressure
- Notch at the bottom of the wellbore for localized initiation
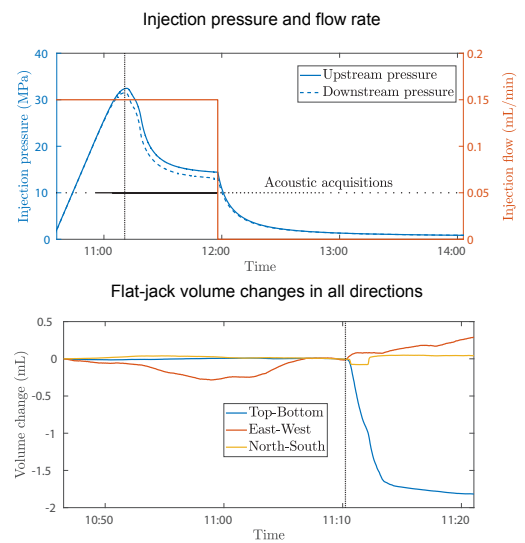- Experiment duration on the order of minutes to a few hours

Needle valve
P_{up} P_{down}
Top
West
East
Bottom

N/S flat-jack pressure controller
E/W flat-jack pressure controller
T/B flat-jack pressure controller

R
D
T

Fracturing fluid
Rubber bladder
Distilled water
Injection pump (ISCO 260D)
Fluid interface vessel

Examples of elastic wave data

Elastic wave signal

P-wave
S-wave
P-wave multiple

Estimation of the fracture opening

Pair 1
Pair 2
Pair 3

Diffracted arrival from fracture tip

HF propagation in a Carmen slate specimen

- Applied stresses: 0.5 MPa vertical, 20 MPa perpendicular to bedding, 2 MPa in remaining horizontal direction
- Injection performed with Glycerol (μ = 0.6 Pa·s), flow rate = 0.6 mL/min
- Toughness-dominated regime of propagation

Injection pressure and flow rate

Upstream pressure
Downstream pressure
Acoustic acquisitions

Flat-jack volume changes in all directions

Top-Bottom
East-West
North-South

Post-mortem photos of the fractured specimen

Part of the fluid-driven fracture surface (perpendicular to bedding)

EPFL

FNSNF
FONDS NATIONAL SUISSE
SCHWEIZERISCHER NATIONALFONDS
FONDO NAZIONALE SVIZZERO
SWISS NATIONAL SCIENCE FOUNDATION

SCCER-SoE Annual Conference 2019

Fluid induced aseismic slip in a Discrete Fracture Network: marginally pressurized vs critically stressed case

Federico Ciardo, Brice Lecampion

Geo-Energy Laboratory - Gaznat chair on Geo-energy, EPFL, Lausanne, Switzerland

Schweizerische Eidgenossenschaft
Confédération suisse
Confederazione Svizzera
Confederaziun svizra

Swiss Federal Office of Energy SFOE

Research context and motivation

Under the **2050 Swiss Energy Strategy**, nuclear power is to be replaced by renewables. In this context, **deep geothermal energy** represents an attractive source of of energy.
A better understanding of **hydro-shearing stimulation** of enhanced geothermal systems is required in relation to **induced seismicity**. To this end, we aim at:
- providing robust numerical tools to simulate hydraulic stimulation of fractured rock masses
- getting insight into the physical governing phenomena, with the ultimately goal of helping engineers during operational decisions.

3-10 Km Depth
Injection well · Production well
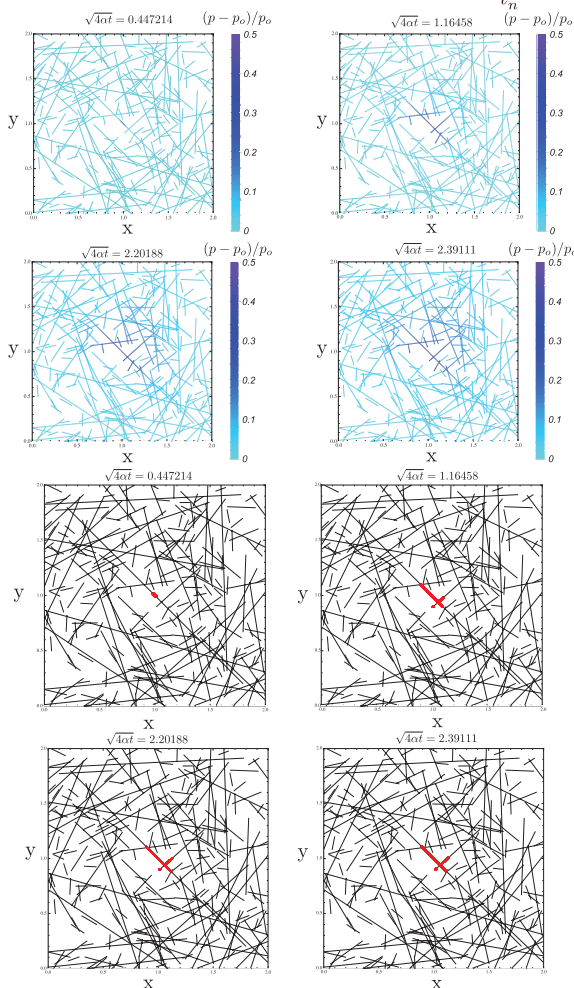Cristalline basement
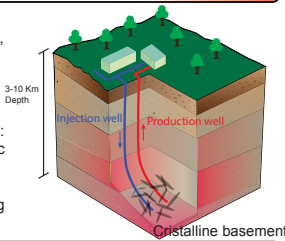
Model assumptions

- Homogenous, isotropic and linear elastic host medium
- Plane strain conditions
- Fractures permeability (constant) way larger than host medium permeability
- No thermal effects and no shear-induced dilatancy
- Neutral friction condition
- Pressure control type of injection (moderate scenario)
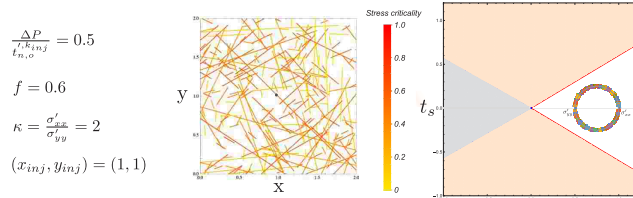
Numerical framework

- Displacement discontinuity method for elasticity (BEM)
- Finite volume scheme for fluid flow
- Hierarchical matrix technique combined with Adaptive Cross Approximation
- One-way coupled HM problem solved with a fully implicit scheme
- Adaptive time stepping based on crack velocity

DFN generation & dimensionless governing parameters

- Power law distribution for fracture length with cut-off for min. and max. fracture lenghts
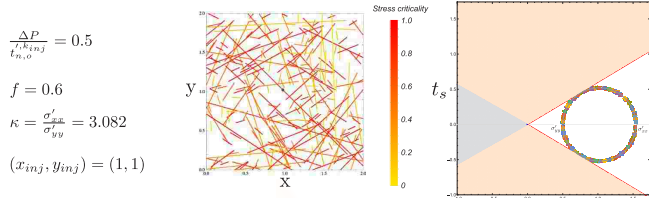- Uniform distribution for fracture location and orientation within the characteristic area

Stress criticality: $\Lambda = \frac{\kappa - 1}{f} \frac{\text{Cot}(\theta)}{(\kappa \text{Cot}(\theta)^2 + 1)}$

Normalized over-pressure at injected fracture k_{inj} : $\frac{\Delta P}{t'_{n,o} k_{inj}}$

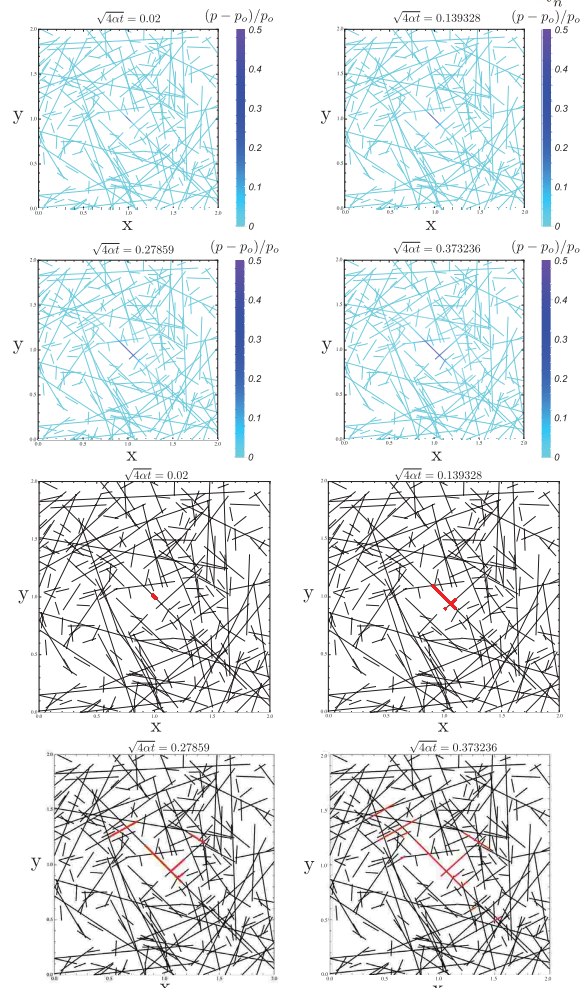## Observations & future perspectives

- For a marginally pressurized DFN, the slipping patch is driven by fluid flow diffusion whose front is located well ahead the slipping patch front.
- On the contrary, for a critically stressed DFN, the fast expansion of slipping patch is mainly driven by stress interaction between fractures. The fluid front is located well inside the slipping patch.
- At which scale a macroscopic fault (shear) zone is created upon fluid injection?

MARGINALLY PRESSURIZED DFN

$\frac{\Delta P}{t'_{n,o} k_{inj}} = 0.5$

$f = 0.6$

$\kappa = \frac{\sigma'_{xx}}{\sigma'_{yy}} = 2$

$(x_{inj}, y_{inj}) = (1, 1)$

Stress criticality

CRITICALLY STRESSED DFN

$\frac{\Delta P}{t'_{n,o} k_{inj}} = 0.5$

$f = 0.6$

$\kappa = \frac{\sigma'_{xx}}{\sigma'_{yy}} = 3.082$

$(x_{inj}, y_{inj}) = (1, 1)$

Stress criticality

OVER-PRESSURE

$\sqrt{4\alpha t} = 0.447214$ $(p - p_o)/p_o$

$\sqrt{4\alpha t} = 1.16458$ $(p - p_o)/p_o$

$\sqrt{4\alpha t} = 2.20188$ $(p - p_o)/p_o$

$\sqrt{4\alpha t} = 2.39111$ $(p - p_o)/p_o$

OVER-PRESSURE

$\sqrt{4\alpha t} = 0.02$ $(p - p_o)/p_o$

$\sqrt{4\alpha t} = 0.139328$ $(p - p_o)/p_o$

$\sqrt{4\alpha t} = 0.27859$ $(p - p_o)/p_o$

$\sqrt{4\alpha t} = 0.373236$ $(p - p_o)/p_o$

ASEISMIC SLIPPING PATCH

$\sqrt{4\alpha t} = 0.447214$

$\sqrt{4\alpha t} = 1.16458$

$\sqrt{4\alpha t} = 2.20188$

$\sqrt{4\alpha t} = 2.39111$

ASEISMIC SLIPPING PATCH

$\sqrt{4\alpha t} = 0.02$

$\sqrt{4\alpha t} = 0.139328$

$\sqrt{4\alpha t} = 0.27859$

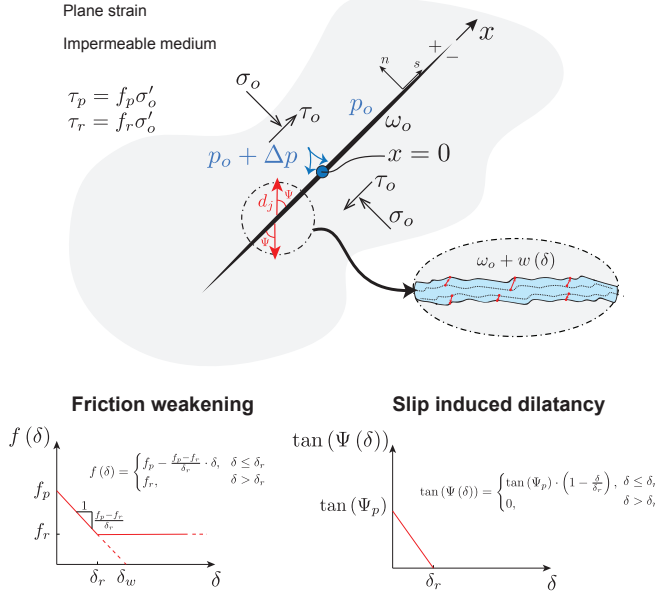$\sqrt{4\alpha t} = 0.373236$

SCCER-SoE Annual Conference 2019

Effect of dilatancy on the transition from aseismic to seismic slip due to fluid injection in a fault

Federico Ciardo, Brice Lecampion

Geo-Energy Laboratory - Gaznat chair on Geo-energy, EPFL, Lausanne, Switzerland

Schweizerische Eidgenossenschaft
Confédération suisse
Confederazione Svizzera
Confederaziun svizra

Swiss Federal Office of Energy SFOE

Model and problem formulation

Plane strain

Impermeable medium

$$\tau_p = f_p \sigma'_o$$
$$\tau_r = f_r \sigma'_o$$

Friction weakening

$$f(\delta)$$

$$f(\delta) = \begin{cases} f_p - \frac{f_p - f_r}{\delta_r} \cdot \delta, & \delta \leq \delta_r \\ f_r, & \delta > \delta_r \end{cases}$$

Slip induced dilatancy

$$\tan(\Psi(\delta))$$

$$\tan(\Psi(\delta)) = \begin{cases} \tan(\Psi_p) \cdot \left(1 - \frac{\delta}{\delta_r}\right), & \delta \leq \delta_r \\ 0, & \delta > \delta_r \end{cases}$$

- Linear elastic equilibrium (quasi-static formulation)

$$t_i(x,t) = t_i^o(x) + \int_{-a}^{a} K_{ij}(\xi,t) \cdot d_j(\xi,t) d\xi, \quad \text{for} \quad i,j = n,s$$

- Shear weakening Mohr-Coulomb yield criterion

$$F(\tau, \sigma'_n) = |\tau| - f(\delta) \cdot \sigma' \leq 0$$

- Non-associated flow rule / Dilatancy

$$\dot{d}_i = \lambda \cdot \frac{\partial G}{\partial t'_i},$$
$$G(\tau, \sigma'_n) = |\tau| - \tan(\psi(\delta))\sigma', \quad \Rightarrow \quad \begin{aligned} \dot{d}_s &= \dot{\delta} = \lambda \cdot \text{sign}(\tau) \\ \dot{d}_n &= \dot{w} = \lambda \cdot \tan(\psi(\delta)) \end{aligned}$$

- Fluid flow ($\alpha = k_f/\mu\beta$ fault hydraulic diffusivity)

$$w_h \beta \frac{\partial p}{\partial t} + \frac{\partial w(\delta)}{\partial \delta} \frac{\partial \delta}{\partial t} + \frac{\partial q}{\partial x} = 0, \quad q = -\frac{w_h \cdot k_f(\delta)}{\mu} \frac{\partial(p - p_o)}{\partial x}$$

- Constant pressure injection condition

$$p(x=0, t) = p_o + \Delta P$$

Fault undrained response

The width averaged fluid mass conservation equation under undrained conditions leads to a pore pressure drop:

$$w_o \beta \Delta p_u + \Delta w = 0 \rightarrow \Delta p_u = -\frac{\Delta w}{w_o \beta} = -\frac{\epsilon_d}{\beta}$$

which leads to a local shear strengthening.

Small scale yielding & ultimate stability

When the half crack length a is much larger than $a_w = \delta_w E'/2\tau_p$, all the strength weakening occur in a small zone near crack tips. The stress intensity factor at complete weakening is thus:

$$K_{II} = (\tau_o - \tau_r)\sqrt{\pi a} + f_r \sqrt{\frac{a}{\pi}} \int_{-a}^{a} \frac{\Delta p(x,t)}{\sqrt{a^2 - x^2}} dx$$

When $a \gg a_w, a \gg \sqrt{4\alpha t}$ & $\dot{a} \gg 0$:

$$\Delta p(x,t) = \Delta P \cdot \delta_{dirac}(x)$$

$$\Delta p(x,t) = \Delta p_u$$

$$\Rightarrow K_{II} \simeq \left(\tau_o - \tau_r + \tau_r \frac{\Delta p_u}{\sigma'_o}\right)\sqrt{\pi a} + f_r \frac{\Delta P}{\sqrt{\pi a}}$$

Taking the limit when $a \to \infty$, a dilatant fault is stable when

$$\boxed{\tau_o < \tau_r^u = \tau_r \left(1 - \frac{\Delta p_u}{\sigma'_o}\right)} \quad \text{Undrained shear strength}$$

Alternatively, this provides a minimum value of dilatancy for a fault stabilization (for a set of in-situ conditions and residual strength)

$$\boxed{\epsilon_d^c = \beta \sigma'_o \left(\frac{\tau_o}{\tau_r} - 1\right)} \quad \text{Critical dilatancy value}$$
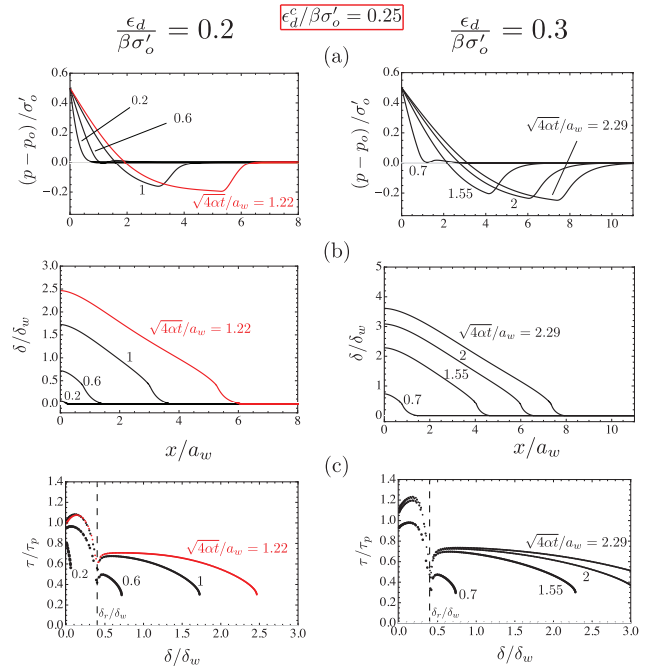
Numerics

- Displacement discontinuity method for elasticity (BEM)
- Finite volume scheme for fluid flow
- Coupled problem solved with a fully implicit scheme
- Adaptive time stepping based on crack velocity

Results - otherwise unstable fault

$$\Delta P/\sigma'_o = 0.5, \qquad \tau_o/\tau_p = 0.75$$
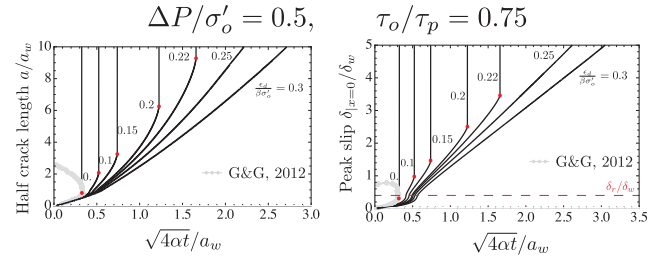
Normalized half crack length a/a_w and peak slip δ/δ_w as function of dimensionless time for an otherwise unstable fault ($\tau_o/\tau_p = 0.75$, $f_r/f_p = 0.6$), subjected to a moderate over-pressure $\Delta P/\sigma'_o = 0.5$.
Effect of the dimensionless dilatancy parameter $\epsilon_d/\beta\sigma'_o$ below and above the critical stabilizing value ($\epsilon_d^c/\beta\sigma'_o = 0.25$ for this case).

$$\frac{\epsilon_d}{\beta\sigma'_o} = 0.2 \qquad \boxed{\epsilon_d^c/\beta\sigma'_o = 0.25} \qquad \frac{\epsilon_d}{\beta\sigma'_o} = 0.3$$

Corresponding spatial profiles of normalized (a) pore pressure changes and (b) slip at different time, below (left) and above (right) the critical value of dilatancy ($\epsilon_d^c/\beta\sigma'_o = 0.25$). Sub-figures (c) show the corresponding evolution of normalized shear strength with slip.

Conclusions

- Dilatancy above a critical value inhibits nucleation of a dynamic rupture for injection pressure sufficient to reach residual friction.
- Dilatancy delays the onset of a dynamic rupture (if occuring) and slows down aseismic crack growth.
- Additional numerical results (not shown here) show that a fault permeability increases with slip accelerate aseismic crack growth but does not affect the stabilizing effect above critical dilatancy.

Reference

Ciardo, F., and Lecampion, B. (2019). Effect of dilatancy on the transition from aseismic to seismic slip due to fluid injection in a fault. *Journal of Geophysical Research: Solid Earth*, 124, 3724-3743.

SCCER-SoE Annual Conference 2019

Schweizerische Eidgenossenschaft
Confédération suisse
Confederazione Svizzera
Confederaziun svizra

Swiss Federal Office of Energy SFOE

Critically-stressed reservoir stimulation direction via stress preconditioning

Barnaby Fryer, Xiaodong Ma, Gunter Siddiqi, Lyesse Laloui

barnaby.fryer@epfl.ch

Motivation

The ability to direct a stimulation treatment in an Enhanced Geothermal System (EGS) well would be a significant advancement for the EGS industry because it would allow for a higher assurance of connectivity (also allowing for larger well separation) and would help avoid known faults.

Previous work has looked at the positive effects of stimulating two wells at the same time (Baria et al., 2004), with a focus on the effect of an elevated pore pressure. Other works have shown the influence of poroelastic effects during stimulation (Jacquey et al., 2018). In this work, these two concepts will be combined and an attempt will be made to guide a stimulation treatment using poroelastic effects from a previous stimulation.

Methods

A sequentially coupled 2-D plane strain poroelastic simulator is employed. A fully implicit finite flow model based on the conservation of mass,

$$\frac{\partial(\phi\rho)}{\partial t} - \nabla \cdot \left(\frac{k}{\mu}\rho\left(\nabla P - \nabla(\rho g z)\right)\right) = q,$$

is used in combination with a finite element mechanical model based on the conservation of momentum,

$$\nabla \cdot \sigma' + \nabla(\alpha P) = -f,$$

and the linear theory of poroelasticity,

$$S_{ij} - \alpha P \delta_{ij} = \frac{E}{(1+\nu)}\epsilon_{ij} + \frac{E\nu}{(1+\nu)(1-2\nu)}\epsilon_{kk}\delta_{ij},$$

The permeability model is based on Miller, 2015 and assumes an orientation of pre-existing potential shear plane in each finite volume cell. Based on this orientation and the stress state, it can be determined if slip is expected. In the event of shear failure, the permeability of cell is assumed to permanently increase by a factor of 200. The reservoir is initially assumed to be critically stressed, such that a Coulomb stress change of 0.1 MPa is enough to induce shear failure.
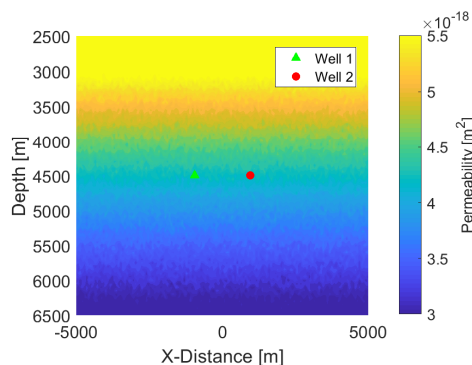
Figure 1: The initial permeability field used. The heterogeneity is due to the randomness associated with the permeability model (Miller, 2015).
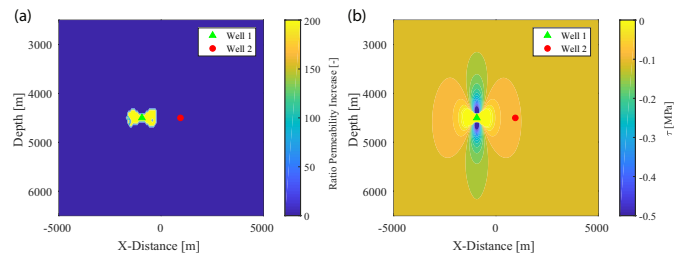
Results

Figure 2: The result of the stimulation of well 1 in the reverse faulting stress regime case. (a) The permeability enhancement associated with the stimulation treatment (t=3 days). (b) The Coulomb stress changes resulting from the stimulation treatment (t=3 days).
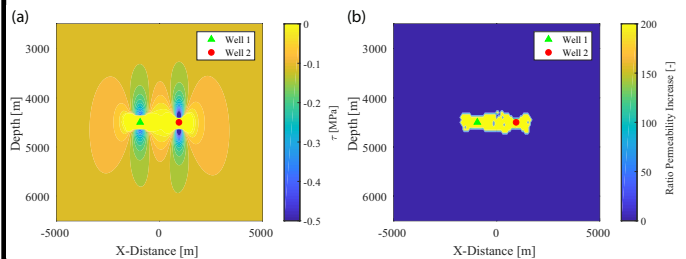

Figure 3: (a) The Coulomb stresses after the stimulation of the second well (t=6 days). (b) The permeability enhancement at the end of the entire procedure (t=6 days). The stimulated zone of each well extends and average 761m away from the other doublet well and 942m towards it.

Conclusion

1) It is suggested that shear stimulation treatments in EGS reservoirs can be directed.

2) Injection-induced poroelastic stress changes are significant in a critically-stressed crust.

3) A methodology which directs shear stimulation treatments in critically-stressed reservoirs using poroelastic stress changes is developed here for all three stress regimes.

References & Funding

[1] Baria, R., Michelet, S., Baumgaertner, J., et al., (2004), Microseismic monitoring of the World's largest potential HDR reservoir.
[2] Jacquey, A., Urpi, L., Cacace, M., Blöcher, G., Zimmermann, G., Scheck-Wenderoth, M. (2018), Far field poroelastic response of geothermal reservoirs to hydraulic stimulation treatment: Theory and application at the Gross Schönebeck geothermal research facility, International Journal of Rock Mechanics and Mining Sciences, 110, 316-327.
[3] Miller, S. (2015), Modeling enhanced geothermal systems and the essential nature of large-scale changes in permeability at the onset of slip, Geofluids, 15, 338-349.

SCCER-SoE Annual Conference 2019

SCCER S SoE
SWISS COMPETENCE CENTER for ENERGY RESEARCH
SUPPLY of ELECTRICITY

Geomechanical response of carbonate-rich Opalinus clay to CO2

Taeheon Kim, Alberto Minardi and Lyesse Laloui

Objective of the research

This research is carried out at the Laboratory of Soil Mechanics at the EPFL within the phase 24 of the CS-C project with the objective of better understanding the caprock material.
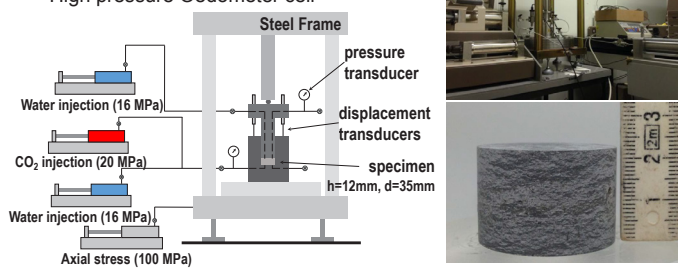
Opalinus Clay (OPA) is often used for studying the behaviour of caprocks as it demonstrates the traits of a proper caprock material for geological CO_2 storage. The OPA samples cored from Mont terri URL contained a thin section of highly concentrated carbonates. Clay-rich OPA was reported to be chemically inert to CO_2, however, since carbonate minerals are highly reactive to acid, the geomechanical response of carbonate-rich OPA (CAR-OPA) to CO_2 was investigated.

To observe the effect of CO_2 on the CAR-OPA, evolution of permeability with CO_2 exposure and spontaneous displacement during CO_2 injection was monitored.

[Experimental scheme]
❑ Apparatus:
High pressure Oedometer cell

Steel Frame
pressure transducer
Water injection (16 MPa)
CO_2 injection (20 MPa)
displacement transducers
specimen h=12mm, d=35mm
Water injection (16 MPa)
Axial stress (100 MPa)

❑ Experimental procedure:
- Pre-exposure phase
1) Saturation of the sample under constant stress state
2) Loading to σ_a = 2.1, 4.3, 8.6 MPa of total axial stress with pore pressure of 1.0 MPa
3) Constant head permeability test each stress state
- CO_2 exposure phase
1) Short-term exposure followed by constant head permeability test
2) Long-term exposure followed by constant head permeability test
3) Injection of CO_2 under σ_a=4.3 MPa
- Post-exposure phase
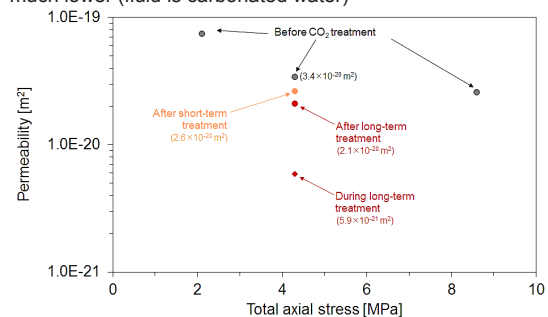1) Reloading-unloading cycles from 4.3 to 8.6 MPa
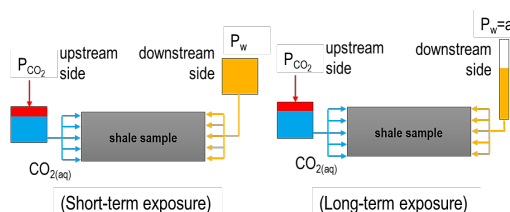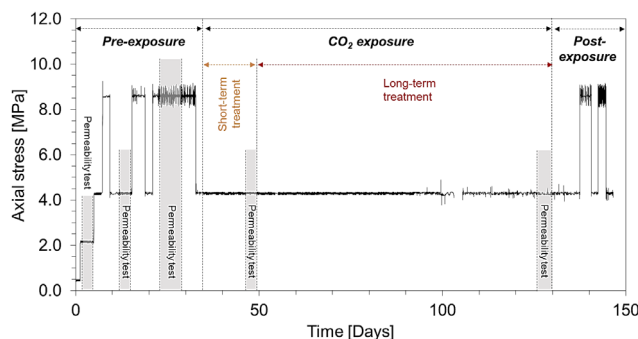
[Results]
❑ Displacement measured during long-term injection
- Compaction continued until the sample flushing stage
- Total compaction 14μm (irreversible)
- Recorded displacement responds sensitive to temperature
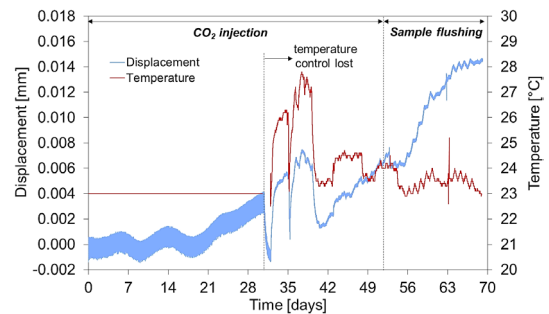
❑ Permeability measurement
- Slight decrease in permeability measurements, using deaerated water, after each treatment
- Permeability measured during the long-term CO_2 injection stage is much lower (fluid is carbonated water)

Before CO_2 treatment
$(3.4×10^{-20}$ m²)
After short-term treatment $(2.6×10^{-20}$ m²)
After long-term treatment $(2.1×10^{-20}$ m²)
During long-term treatment $(5.9×10^{-21}$ m²)

❑ Compression curve pre and post-exposure
- Slightly larger compaction after CO_2 exposure

Primary consolidation:
- Pre-exposure: 12.7μm
- Post-exposure: 14.7μm
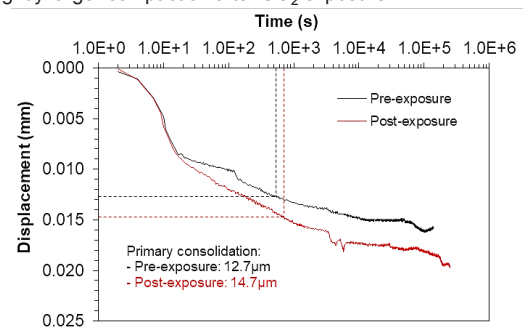
[Discussion]
❑ Permeability measured during the long-term injection can be due to the difference in physical properties (density and viscosity) which the values were unable to measure during the experiment.
❑ The response to temperature may be the response of the sample itself or the system compliance

[Summary]
❑ Permeability was not significantly affected by the CO_2 injection
❑ Irreversible displacement was monitored
❑ Slightly larger compaction after CO_2 exposure
❑ The experiment reacts sensitive to the surrounding temperature

On the seismo-hydro-mechanical response of a shear zone during hydraulic stimulation

H. Krietsch[1], L. Villiger[1], J. Doetsch[1], V. Gischig[2], M.R. Jalali[3] and F. Amann[3]
[1]ETH Zurich, [2]CSD Ingenieure Bern & [3]RWTH Aachen (hannes.krietsch@sccer-soe.ethz.ch)

1. Introduction and monitoring

The experiment was conducted in the framework of the decameter-scale In-situ Stimulation and Circulation (ISC) project in the crystalline rocks at the Grimsel Test Site (GTS), Switzerland. The vertical overburden at the test volume is ~480 m. A comprehensive monitoring system consisting of pressure, strain and seismic monitoring was installed along various boreholes inside the test volume. The here presented hydraulic stimulation experiment targeted a brittle-ductile shear zone (hosted within a meta-basic dyke) for the high pressure fluid injection. The injection volume was 1211 m^3.
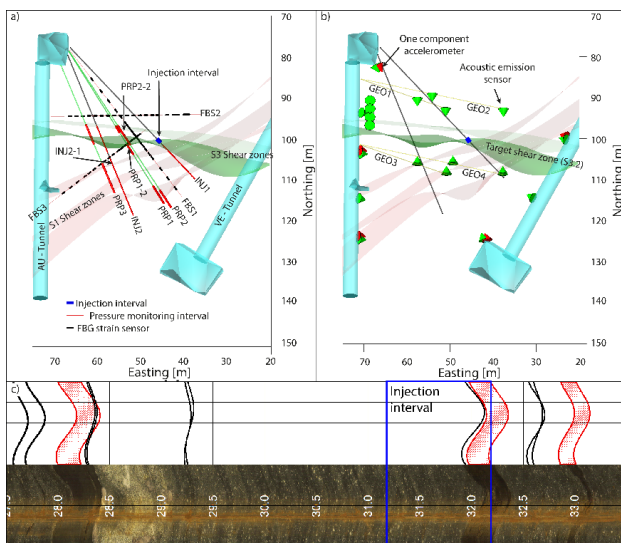
Geological model of ISC test volume with pressure and strain monitoring (a), and seismic array (b). The target shear zone is marked in dark green. The geology of the injection interval is visualized in c).

2. Injection parameters & relation to stress field

The injection consisted of four injection cycles (also see 3. a). The comparison of linear relationships between flow rate and pressure observed for low pressure injection steps during injection cycles 2 and 4 indicate that in-situ injectivity was not increased. Thus, we argue that this stimulation was not successful at the injection well. Nevertheless, hydro-mechanically coupled deformations were dominant at the injection well above 6.1 MPa at the injection well. In addition, injection pressure was limited to ~8 MPa while flow rate was constantly increased. This indicates normal opening (mode I) of the target structures.

Prior to the stimulation experiments the in-situ stress close ('perturbed tensor') to the target shear zone has been characterized. Based on this characterization and geological mapping, stresses across and along the target structures were calculated.

This analysis indicates that there is a higher likelihood for the target shear zone to experience normal opening during high pressure injections at PRP2-2 compared to shear dislocation at PRP1-2.
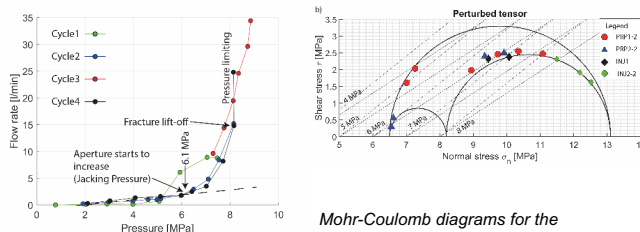

Injection flow rate versus pressure for all four injection cycles.

Mohr-Coulomb diagrams for the perturbed stress tensor (b). Potential failure criteria for different fracture fluid pressures and stress state for the corresponding fractures.

## 3. Hydraulic and seismic rock mass response

The four injection cycles were followed by shut-in phases and venting, during which all pressure lines connected to the test volume were opened. During the first two injection cycles, only minor pressure perturbations and seismicity were detected. The main injection cycle (C3) induced a high pressure perturbation with a steep pressure front in the interval PRP2-2. This pressure perturbation occurred relatively aseismically around this monitoring interval. Most of the seismic events appeared towards the interval PRP1-2 during C3. With ongoing stimulation (C4), the seismic front propagated continuously towards PRP1-2 and away from the injection interval INJ1-2. Additionally, a high pressure perturbation arrived at the interval PRP1-2, while interval PRP2-2 was not pressurized again.
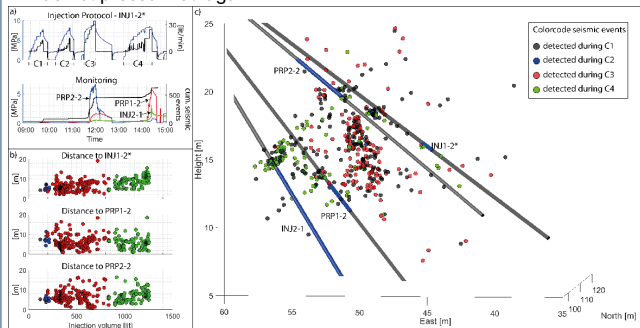
Visualization of injection protocol, monitored pressure and seismicity over time (a), and the relationship between injected fluid volume and distance between seismic event and pressure monitoring interval (b). View onto the target shear zone with pressure intervals and seismic events (including timing).

4. Schematic interpretation

Two different high pressure signals propagated along the target shear zone during the fluid injection. The first signal is characterized by a steep pressure front, mostly aseismic deformation and did not re-occur during the subsequent injection cycles (C4). This signal propagated upward towards east during C3. The stress field indicated that this pressure signal was coupled with normal opening (mode I) of the target shear zone. The second pressure signal consisted of a less steep pressure front during C3 and enhanced pressure signal during the subsequent injection cycle (C4). Based on the stress field, this pressure signal might be coupled with shear dislocation. This is consistent with the observed seismicity , which propagated in the same direction as the second pressure signal downwards towards east. Note that the peak pressure (P$_{peak}$) is higher for the first pressure signal, compared to the second one.
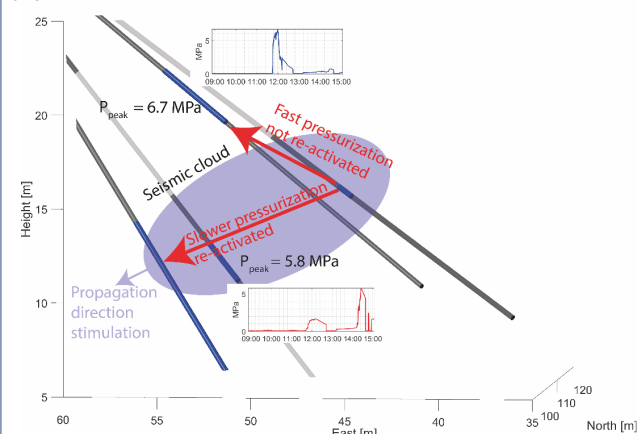
View onto the target shear zone. The pressure monitoring intervals are visualized with the obtained peak pressures. The pressure signals, the seismic cloud and the propagation direction of the stimulation direction are drawn schematically.

SCCER–**SoE**
SWISS COMPETENCE CENTER for ENERGY RESEARCH
SUPPLY of ELECTRICITY

EPFL

SCCER-SoE Annual Conference 2019

Laboratory hydraulic fracturing tests in low-permeability rocks

Liu, D., Blum, T. & Lecampion, B.
Geo-energy Lab, Gaznat Chair on Geo-Energy,
EPFL, Lausanne, Switzerland

GeoEnergyLab

1. Abstract

We aim to investigate the effect of grain size (corresponding to different process zone sizes) on the propagation of hydraulic fractures. We use active acoustic monitoring to track the evolution of the fracture radius and fluid thickness. We present preliminary results of a toughness-dominated experiment in Gabbro and a lag-viscosity dominated experiment in Marble.

2. Experimental set-up
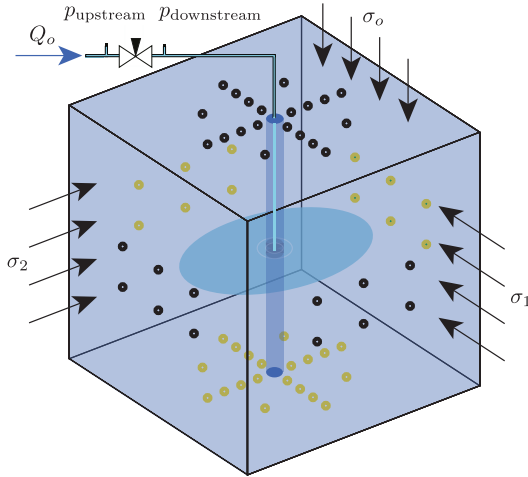
Fig. 1 Schema of the tested rock block (25x25x25 cm³) under true tri-axial confinement and fluid injection, along with the transducer disposition
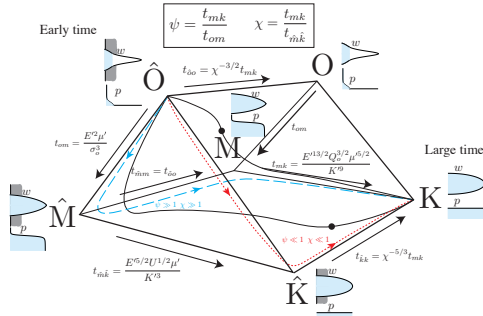
3. Experimental Design

Fig. 2 Schematic evolution of the initiation and propagation of radial hydraulic fracture from a wellbore in dimensionless space [1].

$$\psi = \frac{t_{mk}}{t_{om}} \qquad \chi = \frac{t_{mk}}{t_{\hat{m}k}}$$

$$\mu' = 12\mu \qquad E' = \frac{E}{1-\nu^2} \qquad K' = \sqrt{\frac{32}{\pi}}K_{Ic}$$

Table. 1 Material parameters for gabbro and marble

Rock	grain size (mm)	E(GPa)	ν	K_{Ic}(MPa.$\sqrt{m}$)	ρ(g/cm³)	V_p(km/s)
Gabbro	1-3	68.4	0.31	3.33	3.05	6.76
Marble	0.1-0.2	69.4	0.29	1.83	2.69	6.09

Table. 2 Sample configuration and tests parameters for different experiments

Rock	Wellbore radius (mm)	Initial defect length (mm)	σ_o(MPa)	$\sigma_1 = \sigma_2$(MPa)	μ(Pa.s)	Q_o (mL/min)	U (mL/GPa)
Gabbro	7.5	3	0.5	10.5	0.6	0.2	217.3
Marble	7.5	3	10	20	100	0.2	282.5

Table. 3 Viscosity-toughness transition time scales and dimensionless parameters

Rock	t_{mk}(s)	$\psi = \frac{t_{mk}}{t_{om}}$	$\chi = \frac{t_{mk}}{t_{\hat{m}k}}$	$\mathcal{L} = \ell_o/(E'U)^{1/3}$	$\mathcal{A} = a/(E'U)^{1/3}$
Gabbro	7.34×10^{-4}	2.28×10^{-9}	1.72×10^{-4}	0.0118	0.029
Marble	6.32×10^{5}	9.18	12.5	0.0108	0.027

d.liu@epfl.ch

4. Preliminary results

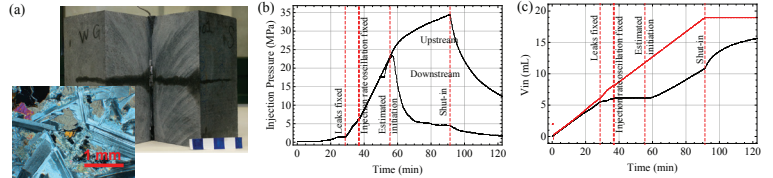### 4.1 Absolute Black Gabbro (Zimbabwei)

Fig. 3 a) Thin section of the gabbro and post mortem photo of the block (in the white-blue color bar, each square is 2x2 cm²), b) Evolution of the upstream and downstream injection pressure, c) Evolution of the volume injected by the pump (red) and the volume entering into the fracture (black).
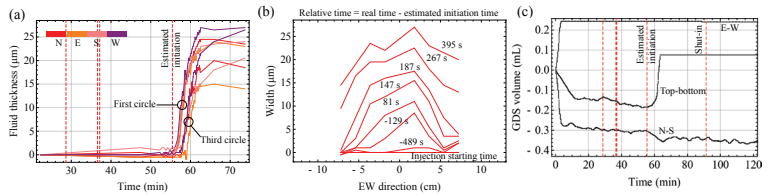

Fig. 4 a) Evolution of the fluid thickness corresponding to the transducers in the first and third circle nearest to the wellbore, b) Evolution of the fracture width profiles in the east-west direction at the relative time (real time substracted by the estimated intiation time using pressure and GDS data, c) Evolution of the GDS pump volume.
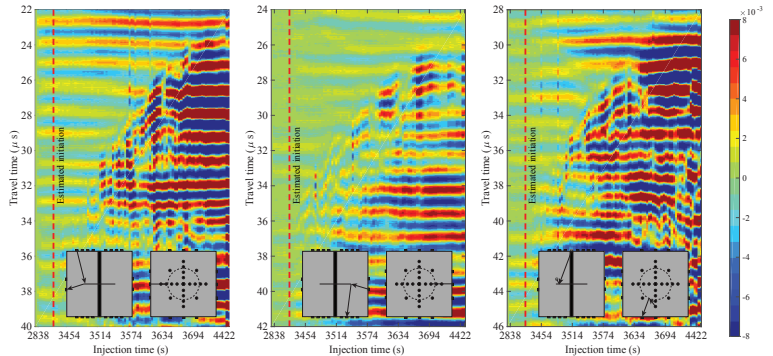

Fig. 5 Data in the difference domain for a pair of P-wave transducers (P-wave source to diffraction to P-wave receiver, PdP), along with the acquisition geometry.
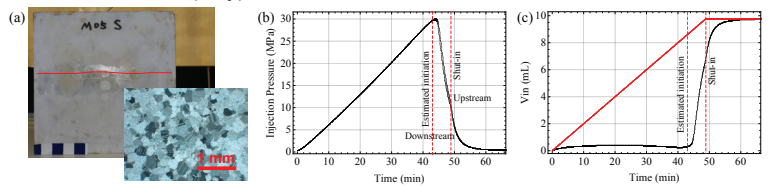
4.2 Carrara Marble (Italy)

Fig. 6 a) Thin section of the marble and post mortem photo of the block (in the white-blue color bar, each block is 2x2 cm²), b) Evolution of the upstream and downstream injection pressure c) Evolution of the volume injected by the pump (red) and the volume entering into the fracture (black).
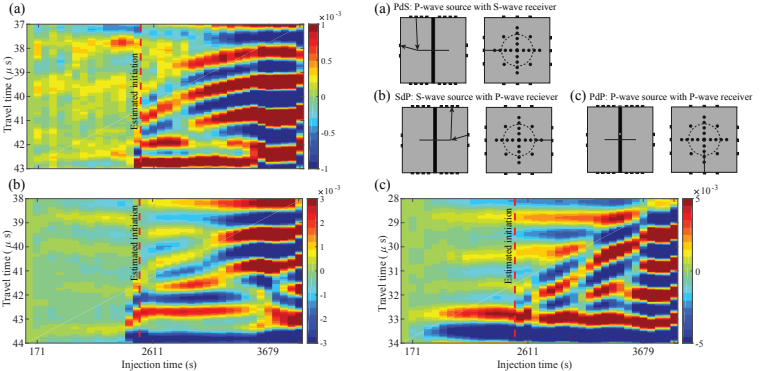

Fig. 7 Data in the difference domain for one P-wave transducer and one S-wave transducer (a, b), and a pair of P-wave transducers (c), along with the acquisition geometry.

1. Lecampion, B., Desroches, J., Jeffrey, R. G., & Bunger, A. P. (2017). Experiments versus theory for the initiation and propagation of radial hydraulic fractures in low-permeability materials. Journal of Geophysical Research: Solid Earth, 122(2), 1239-1263.
2. J. Groenenboom, Acoustic monitoring of hydraulic fracture growth, PhD thesis, TU Delft, Deltft Univeristy of Technology (1998).

Fluid injection driven, a-seismic fracture growth with remote nucleation on heterogeneous fault

Andreas Möri, Brice Lecampion* and Federico Ciardo
Geo-Energy Lab - Gaznat chair on Geo-energy, EPFL, Lausanne, Switzerland
*Contact: brice.lecampion@epfl.ch

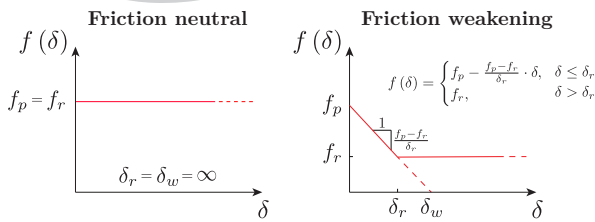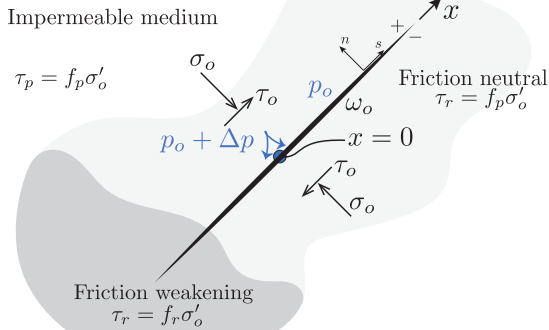Schweizerische Eidgenossenschaft
Confédération suisse
Confederazione Svizzera
Confederaziun svizra

Bundesamt für Energie BFE
Swiss Federal Office of Energy SFOE

1. Model and problem formulation

Plane strain
Impermeable medium

$\tau_p = f_p \sigma'_o$

Friction neutral
$\tau_r = f_r \sigma'_o$

Friction weakening
$\tau_r = f_r \sigma'_o$

Friction neutral

$f(\delta)$

$f_p = f_r$

$\delta_r = \delta_w = \infty$

Friction weakening

$f(\delta)$

$f(\delta) = \begin{cases} f_p - \frac{f_p - f_r}{\delta_r} \cdot \delta, & \delta \le \delta_r \\ f_r, & \delta > \delta_r \end{cases}$

$\frac{1}{\frac{f_p - f_r}{\delta_r}}$

$\delta_r \quad \delta_w$

- Linear quasi-static elasticity

$$t_i(x,t) = t_i^o(x) + \int_{-a}^{a} K_{ij}(\xi,x) \cdot d_j(\xi,t) \mathrm{d}\xi, \text{ for } i,j = n,s \quad (1)$$

- Constant pressure injection condition / constant fault permeability case

$$p = p_o + \Delta p \quad (2)$$

We assume $p_o + \Delta p$ remains below fault opening pressure (σ^o).

2. Numerics

- Displacement discontinuity method for elasticity (BEM)
- Finite volume scheme for fluid flow
- Fully coupled implicit solver (HFPx2D) developed at EPFL
- Adaptive time stepping based on current crack velocity

3. Theoretical developments

A linear relation between the crack half length and the position of the fluid pressure front due to pore pressure diffusion along the fault exists. Defining the dimensionless half-crack length $\gamma = \ell/\sqrt{4\alpha t}$ (with α the fault diffusivity), using the solution for 1D diffusion and stating that $\tau(\xi) = \tau_p$ inside the crack, the elasticity equation reduce for a planar fault to:

$$\frac{\tau(\xi) - \tau_o}{f_p \Delta p} \overset{\tau(\xi) = \tau_p}{=} \underbrace{\frac{\tau_p - \tau_o}{f_p \Delta p}}_{T} = \mathrm{Erfc}|\gamma\xi| - \frac{1}{2\pi}\int_{-1}^{+1}\frac{\mathrm{d}\bar{\delta}}{\mathrm{d}\eta}\frac{\mathrm{d}\eta}{\xi - \eta} \quad (3)$$

Dimensionless parameter T balances stress criticality (prior to the injection) and magnitude of the over-pressure. Asymptotic solution following [Viesca R., pers. comm., September 2018] serve as benchmark for the numerical solvers.

6. Conclusions

- A-seismic crack tip and pore pressure front can significantly differ:
  - marginally pressurized (fluid pressure front $\gg$ aseismic crack front)
  - critically stressed (aseismic crack front $\gg$ fluid pressure front)
- Critically stressed faults with a weaker frictional weakening part can exhibit remote activation (far away from the pore-pressure disturbance), i.e. activation of a daughter crack with a possible subsequent nucleation of a dynamic rupture
- The dynamic nucleation lengthscale of the daughter crack scales as $a_w = \delta_w E'/(2\tau_p)$ following [Uenishi, K., and J.R. Rice (2003), Garagash, D. and Germanovich, L. (2012)] (linear frictional weakening).

4. Benchmark
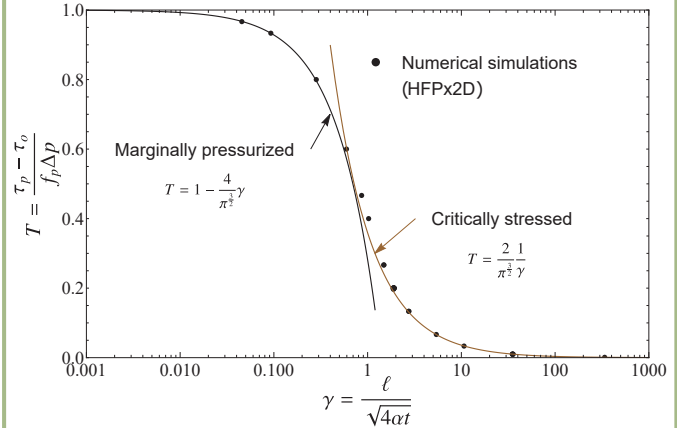
Dimensionless a-seismic fracture length γ as function of T. Numerical results are displayed as dots, analytical asymptotes for the marginally pressurized and critically stressed cases as continuous lines [Viesca, pers. comm., September 2018]

5. Remote activation on weaker part of fault
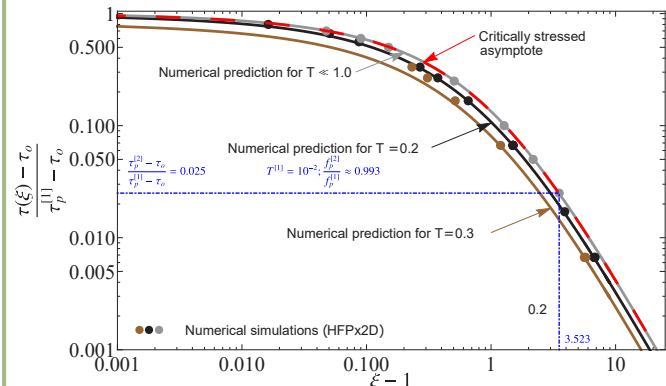
Stress perturbation ahead of aseismic mother crack tip (superscript [1]) for critically stressed cases, where $\xi = \frac{x}{\ell^{[1]}}$. This can lead to a remote activation of a daughter crack (superscript [2]), on a heterogeneity with lower strength, possibly nucleating dynamically (if frictional weakening occurs).
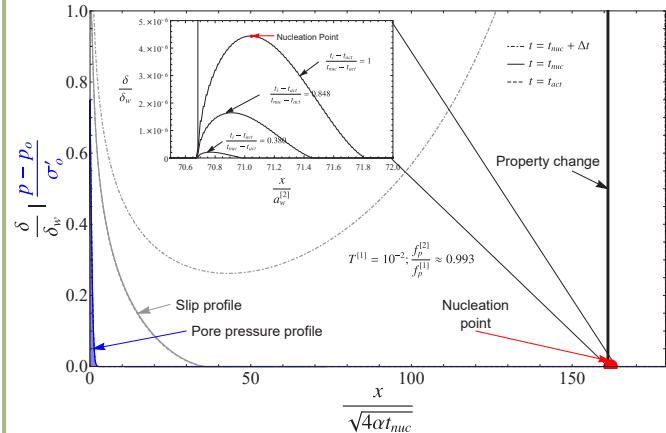
Slip profiles (gray) and pore pressure (blue) in function of normalized line coordinate. Inset shows slip evolution within the daughter crack. Nucleation in daughter crack scales with $a_w^{[2]}$.

- Friction neutral fault properties at injection
- Frictional weakening part with lower peak friction coefficient (i.e. $f_p^{[1]} > f_p^{[2]}$)
- Stress transfer dominated regime
- Remote activation of a-seismic slip with possible nucleation

Hydraulic fracture in transversely isotropic material: propagation perpendicular to the isotropy plane

Fatima-Ezzahra Moukhtari, Brice Lecampion

Geo-Energy Laboratory - Gaznat Chair on Geo-Energy (GEL),

Ecole Polytechnique Fédérale de Lausanne (EPFL)

fatima-ezzahra.moukhtari@epfl.ch, brice.lecampion@epfl.ch

Motivation

Transverse isotropy (TI) is an intrinsic characteristic of most sedimentary rocks, especially mudstones. We investigate here how TI anisotropy influence the growth & shape of planar 3D hydraulic fractures (HF). We focus on the case of propagation perpendicular to the plane of isotropy (i.e. bedding plane): a configuration encountered for normal / strike-slip stress regimes with horizontal bedding planes for which the normal stress to bedding or/and the bedding planes strength are sufficient to favor propagation perpendicular to the material isotropy plane. A practical situation for HF growth in unconventional reservoirs.

Near tip elastic modulus

Coupling between lubrication flow and LEFM yields a complex multiscale behavior near the tip of a hydraulic fracture [1]. The near-tip asymptotic solution is based on a plane-strain configuration which for a TI material depends on the local direction of propagation e_1' with: $\widehat{e_1, e_1'} \equiv \alpha$. In such a local plane-strain frame, the near-tip elastic relation is similar to the isotropic case, pending the use of a plane strain elastic modulus E'_α function of the local propagation direction.
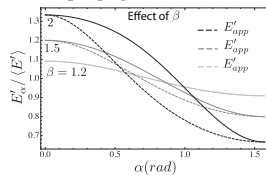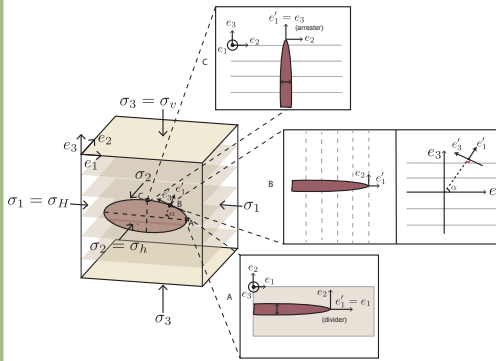

Figure 1: Local near-tip elastic modulus as function of propagation direction (α). E'_α also depends on 5 elastic constants: $\langle E' \rangle = (E'_\alpha(0) + E'_\alpha(\pi/2))/2$, $\beta = E'_\alpha(0)/E'_\alpha(\pi/2)$, Thomson parameters ($\epsilon, \delta$) and the ratio C_{13}/C_{11}. Approximation proposed by [3] in dashed lines. Other constants $\epsilon = 0.3$, $\delta = 0.2$, and $C_{13}/C_{11} = 0.5$.

Numerical scheme

We extend the implicit level set algorithm (ILSA) to account for anisotropy of both elastic properties and fracture energy [2]. This numerical scheme combines a finite discretization for the non-linear coupling of elasticity and lubrication flow (using boundary element method for elasticity discretization and finite volume method for fluid flow) and the near-tip hydraulic fracture asymptotes to evolve the fracture front. The extension to anisotropy notably requires the addition of an iterative loop to resolve the local propagation direction of the fracture all along its perimeter - i.e. in order to use the proper near-tip modulus (see Figure 1) and fracture toughness in the near-tip HF asymptote.
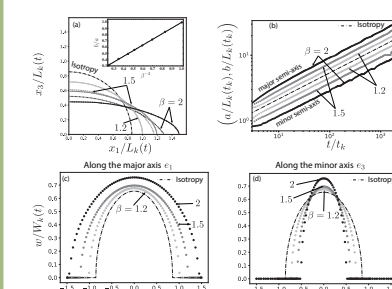
Problem formulation

- TI Elasticity (mode I planar fracture)

$$p_f(y_1, y_3) - \sigma_h =$$
$$-c_{22mn} \int_S \frac{\partial S_{22}^m(\boldsymbol{y}, \boldsymbol{x})}{\partial x_n} w(\boldsymbol{x}) \, dx_1 dx_3$$

- Lubrication flow

$$\frac{\partial w}{\partial t} + \nabla \cdot \mathbf{q} = \delta(x_1, x_3) Q_o$$
$$\mathbf{q} = -\frac{w^3}{12\mu} \nabla(p_f - \rho_f g \delta_3)$$

- Propagation condition (along the front)
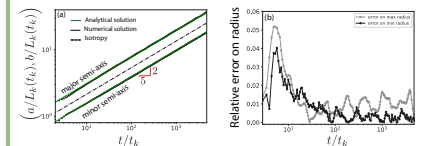
$$K_I = K_{Ic}(\alpha)$$

Planar hydraulic fracture propagating perpendicular to the isotropy plane (e_1, e_2) of a TI impermeable elastic media under constant point-source injection (rate Q_o). w denotes the fracture width, p_f the fluid pressure and $\mathbf{q}$ the fluid flux. Insets correspond to the variation of the near-tip plane-strain configuration along the fracture front as function of the angle α with the isotropy plane.

Viscosity regime
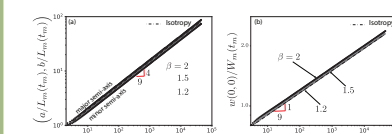
Figure 2: Small effect of TI elasticity in viscosity regime. a) semi-axis time evolution, and b) width at the injection function of time ($\epsilon = 0.3$, $\delta = 0.2$, $C_{13}/C_{11} = 0.5$). Penny-shaped HF M-scaling (L_m, W_m) [1].

Toughness regime / Elastic TI only

Figure 3: Horizontal elongation of the fracture due to TI. a) Self-similar (1/4) footprint, b) semi-axis time evolution, and c,d) self-similar width profiles along principal axis ($\epsilon = 0.3$, $\delta = 0.2$, $C_{13}/C_{11} = 0.5$). Penny-shaped HF K-scaling (L_k, W_k) [1].

Toughness regime / TI & Anisotropic K_{Ic}

"Elliptical" evolution of fracture toughness:

$$K_{Ic} = K_{Ic,3} \left(\frac{E'_\alpha}{E'_3}\right) \left(\sin^2 \theta + \left(\frac{\kappa}{\beta}\right)^4 \cos^2 \theta\right)^{1/4}$$

$$\theta = \arctan\left(\frac{\kappa \tan \alpha}{\beta}\right), \qquad \kappa = K_{Ic,1}/K_{Ic,3}$$

$$b(t) = \left(\frac{3tQ_o E'_3}{8 K_{Ic,3} \sqrt{\pi}} \gamma\right)^{2/5}, \quad a(t) = \left(\frac{K_{Ic,3}}{K_{Ic,1}} \frac{E'_1}{E'_3}\right)^2 b(t).$$

Figure 4: Verification - toughness dominated elliptical HF: $\kappa^{-1} = 1.2$, $\beta = 1.2$, $\epsilon = 0.3$, $\delta = 0.2$, and $C_{13}/C_{11} = 0.5$. (a) Time-evolution of the dimensionless minor and major axis, and (b) relative error compared to the toughness dominated analytical solution derived in [4].

References

[1] E. Detournay. Mechanics of hydraulic fractures. *Annual Review of Fluid Mechanics*, 48:311–339, 2016.

[2] H. Zia, B. Lecampion and W. Zhang Impact of the anisotropy of fracture toughness on the propagation of planar 3D hydraulic fracture. *Int. J. Frac.*, 211(1-2): 103-123, 2018.

[3] H. Laubie and F.J. Ulm Irwin's conjecture: Crack shape adaptability in transversely isotropic solids. *J. Mech. Phys. Sol.*, 68: 1-13, 2014.

[4] F.E. Moukhtari, B. Lecampion, and H. Zia Propagation of a planar hydraulic fracture perpendicular to the isotropy plane of a transversely isotropic material. No. CONF. 53rd US Rock Mechanics/Geomechanics Symposium, 2019.

EPFL

A fast 3D BEM solver for fracture mechanics

Schweizerische Eidgenossenschaft
Confédération suisse
Confederazione Svizzera
Confederaziun svizra

Bundesamt für Energie BFE
Office fédéral de l'énergie OFEN

Carlo Peruzzo, Elizaveta Gordeliy, Dmitry Nikolskiy, Brice Lecampion, François Fayard

Geo-Energy Laboratory - Gaznat chair on Geo-Energy, EPFL, Lausanne, Switzerland

Motivation

Hydraulic fractures are mainly employed in geomaterials in order to increase the productivity of wells. They are used in geothermal energy and oil and gas production to increase the permeability of porous formation either for enhanced fluid production or storage (CO_2 storage).

They are created by engineering fluid injection from deep wellbores. The propagation of an hydraulic fracture is a coupled nonlinear problem where the elasticity of the rock is coupled with the fluid flow through the fracture channel and the porous formation. The coupling with the fluid flow requires the elasticity to be solved multiple times and so, a very fast and efficient solver for linear elastic fracture propagation is required.

Solver Description

The solver uses a displacement discontinuity Boundary Element Method (BEM) to solve for quasi-static elasticity. It allows to discretize only the 3D fracture surfaces avoiding the discretization of the surrounding 3D space required by other techniques such as Finite Element Method (FEM). On one hand this is an advantage because the resulting matrix, that has to be inverted to solve the linear problem, is much smaller compared to the one obtained via FEM (given the same goal error of the numerical solution). On the other hand, the major drawbacks of BEM are that the influence matrix is fully populated and, in the general case, non-symmetric. The first drawback leads to a large memory cost and the latter to an increase of the computational cost of the solution. The implementation described here tackle both problems by taking advantage from the spatial decay of the elastic kernel: the influence of a given displacement discontinuity (DD) at one source point on the traction at the observation point, decays as $1/d^2$, where "d" is the distance between them. We use a hierarchical matrix approach to approximate the original matrix [3-5]. This method can be summarized via two complementary methodologies: i) a cluster tree of the mesh (which depth is controlled by a parameter M) combined with an admissibility condition (controlled by a parameter η) decides which sub-block can be approximated as low-rank ii) the low-rank approximation is performed via adaptive cross approximation for speed (whose accuracy is controlled by ε).

Finally, the results presented here have been obtained using piece-wise quadratic triangular DDs element and ran on MacBook Pro (2017) i5 2.3GHz with 8GB of RAM.

Penny shaped crack

Uniform convergence studies

The numerical solution has been obtained for a penny shaped crack of a radius R=1.5, using a series of different meshes shown on the Figure 3. The elastic parameters used are G=1000 (shear modulus) and v=0.1 (Poisson ratio). $\varepsilon=10^{-5}$ and M=500 has been assumed for all the computations. The figures below are showing the L_2 norm of the relative error in the crack width (Figure 5), the relative error of stress intensity factor (Figure 6), the creation time of the H matrix approximation (Figure 7) and the compression ratio achieved in each simulation vs. number of degrees of freedom (Figure 4). This result show that one can use a large value of η (e.g. η=10) without any reduction in the accuracy of the numerical solution. Beside that the computational cost and the storage requirements are significantly reduced.
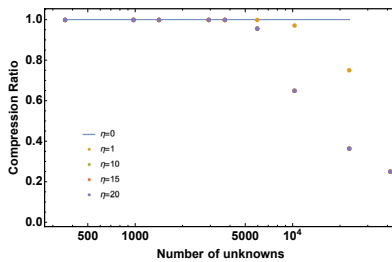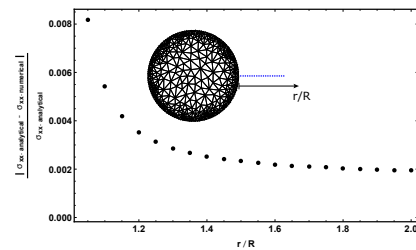
Figure 4: Compression ratio of the hierarchical matrix.

Stress verification

The numerical solution for the stress has been verified against the analytical solution for the stress around the penny shaped crack [1].

Figure 1: Comparison of the σ_{xx} with the analytical solution [1]. The inset of the figure is showing the location of the observation points (in blue) at which the stresses have been computed.

elements	15	54	79	163	206	331	569	1276	2308
unknowns	360	972	1422	2934	3708	5958	10242	22968	41544

Figure 3: series of different uniformly distributed meshes.

Crack opening verification

The numerical solution for the crack opening has been obtained for a uniform mesh and a non-uniform mesh refined at the crack front.

These results suggest that it is more efficient to use a non-uniform mesh refined at the crack front than a uniform mesh, for the same number of unknowns : 14220.
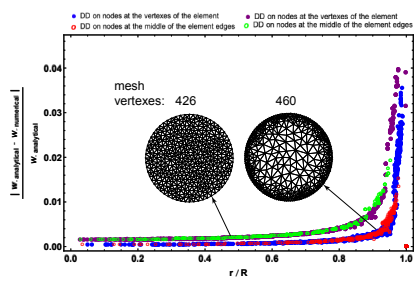
Figure 2: Relative error in crack width, obtained using a uniform and a non-uniform mesh refined at the crack front.
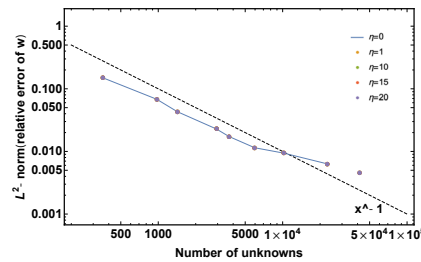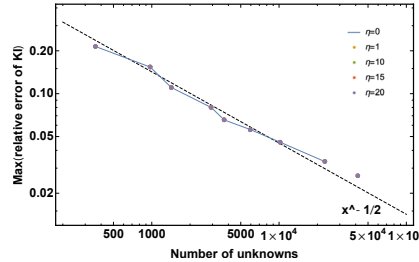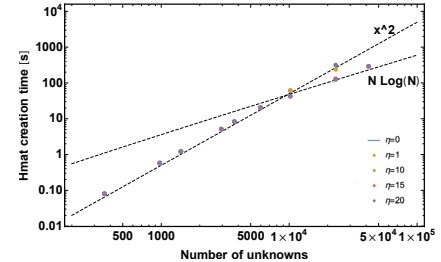
Figure 5: L_2 norm of the error of the crack opening.

Figure 6: Max of the relative error on the stress intensity factor K_I

Figure 7: Hmat creation time vs. number of unknows.

Bowl-shaped crack (Mixed Mode Fracture)

A bowl-shaped crack of radius R = 1.5 and α=60º (see Figure 8) has been discretized with 890 triangular elements (see figure 9), leading to a system with 14760 unknowns. The elastic parameters that characterize the isotropic and elastic medium are G=1000 (shear modulus) and v=0.1 (Poisson's ratio). The crack has been loaded with a uniform unit pressure. The solution obtained with the presented code, has been compared against a numerical solution obtained with an axisymmetric Displacement Discontinuity method. The comparison between the normal opening and the relative error is shown in figures 10 and 11 respectively.
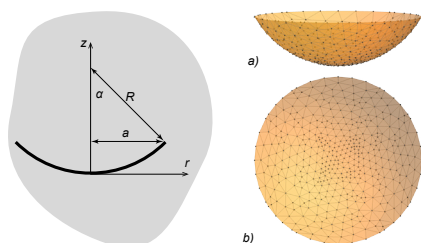
Figure 8: Cross-section of a bowl-shaped crack in an infinite space.

Figure 9: Lateral view a) and top view b) of the discretized bowl-shaped crack.
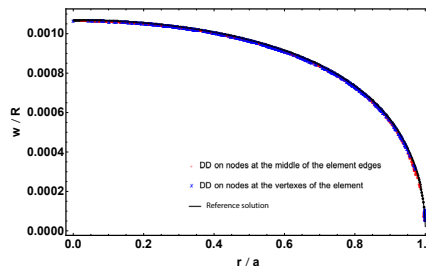
Figure 10: Bowl-shaped crack. Comparison of the crack normal opening (w) scaled with the crack radius R with a numerical solution obtained with an axisymmetric Displacement Discontinuity code [2].
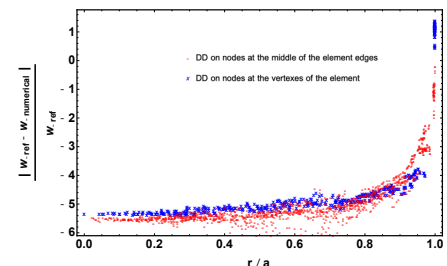
Figure 11: Bowl-shaped crack. Relative difference between the crack widths (w) obtained with the axisymmetric Displacement Discontinuity code [2] and the present code Hfp-3D.

References

[1] Nikolskiy, D.V., Mogilevskaya, S.G. & Labuz, J.F. (2013). *Complex variables boundary element analysis of three-dimensional crack problems.* Engineering Analysis with Boundary Elements, 37(11), 1532-1544.

[2] Gordeliy, E. & Detournay, E. (2011). *Displacement Discontinuity Method for Modeling Axisymmetric Cracks in an Elastic Half-Space.* International Journal of Solids and Structures, 48, 2614-2629.

[3] Hackbusch. W., (1999). *A sparse arithmetic based on H-Matrices. Part I: Introduction to H-Matrices.* Computing, 62, 89-108.

[4] Chaillat S., Desiderio L. & Ciarlet P. (2017). *Theory and implementation of H-matrix based iterative and direct solvers for Helmholtz and elastodynamic oscillatory kernels.* Journal of Computational Physics, 351, 165–186.

[5] Benedetti, L., Aliabadi, M.H. & Davi, G. (2008). *A fast 3D dual boundary element method based on hierarchical matrices.* International Journal of Solids and Structures, 45, 2355-2376.

SCCER-SoE Annual Conference 2019

Small Flex

Added value of smart storage operations on an alpine run-off-river HPP obtain from hydrological-hydraulic modelling

Maria Ponce, Jessica Zordan*, Pedro Manso , Cécile Münch
Laboratory of Hydraulic Construction (LCH), École Polytechnique Fédérale de Lausanne (EPFL), Switzerland
*Corresponding author: jessica.zordan@epfl.ch

EPFL

Framework

Run-off-river hydro projects can create sustainable energy minimizing impacts to the surrounding environment. Among many advantages of these systems, whose development has in fact been largely supported during the past years by the confederation, their main limitation is that their functioning is dependent by the available discharge, as they do not have storage. In order to overcome this constrain and enhance their flexible use, the Smart Storage Operations (SSO) are introduced (Figure 1c). SSO consist on using temporarily some existed underground structures of the power plant, such as the settling basin, for water storage. This water can be used afterward to produce peak energy timed with the demand. This is particularly useful since it allows water accumulation in periods of the year when the discharge is too low for energy production, therefore minimizing water losses.

The aim of this study was to create a hydrological-hydraulic model in order to reproduce the HPP operations (both under normal use - Figure 1b - and SSO - Figure 1d). The elaborated framework was applied at the hydropower plant KW Gletsch-Oberwald (Figure 1a) located at Valais (Switzerland) but it can be applied to others HPP in the Alpine region with dominant glacier cover, or areas with an intermittent river. A validation of the model was possible thanks to the measurements which were collected at the HPP during one week of site tests.
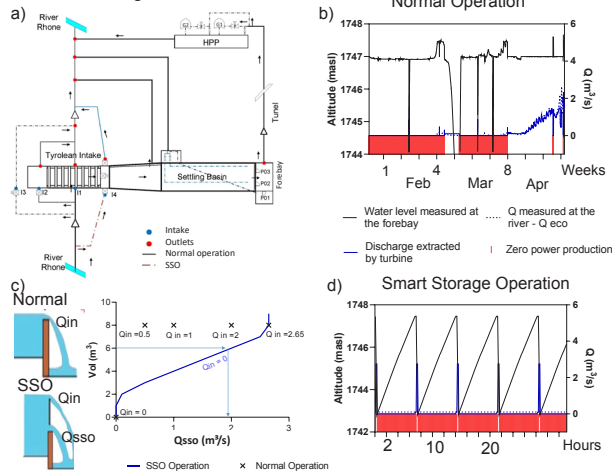

Figure 1: a) Schematic representation of the water infrastructure, and b) Measured water level at the forebay and turbine inflow during a normal operation at KW Gletsch-Obwerwald, c) Discharge and turbine inflow during the SSO operation, and d) Water level at the forebay and turbine inflow during a SSO.

Methods

RS Minerve was the computational selected tool. It allows to create a combined hydrologic and hydraulic model in a semi-distributed conceptual scheme. For the **hydrology model**, the snowmelt, glacier melt, snow accumulation and runoff process are reproduced by empirical models on daily base. The output was downscaled on an hourly basis, using climatic historical data of 28 years (Grimsel station). The **hydraulic model** was validated for normal operations and SSO using measured data.

These two models were joined to conform to a unique model. To evaluate the SSO, a yearly simulation was performed estimating the energy production and determining the economic revenues and the additional economic value of SSO with respect to normal operations.
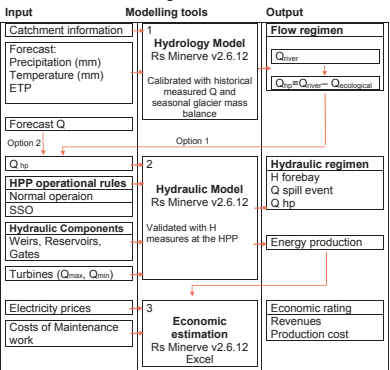

Figure 2: Flowchart of the methodology used.

Results and discussion

On this catchment of 39 km², the glacier (52% of the basin) and snowmelt have a direct influence in the hydrology. The final hourly calibration by the multi-objective function using 14 years (2005-2018) of measured discharge at Gletsch gave a performance indicator of Nash equal to 0.89 and a Relative Volume Bias of 1,1 e-3. The Figure 2b showed a good correspondence with the measured data.

The hydraulic model was validated with the measured water level inside the forebay tank, during normal operations, for winter 2017-2018 and the SSO for with the measurements collected during the site tests in November 2018. Both models showed a good correspondence with a Nash equal to 0.96 and 0.85 respectively.

With the validated simulations of the Normal and SSO, it was possible to reproduce in detail the SSO in a week of 2018 and for a complete year.

The simulation approach with the proposed framework proved an evident increment of power productions for the season with lower discharge (winter season), that goes from 50 to 100 %, depending on the inflow (when the inflow is less than the minimum discharge for one turbine, the HPP would need to switch off, therefore the gain goes up to 100%).
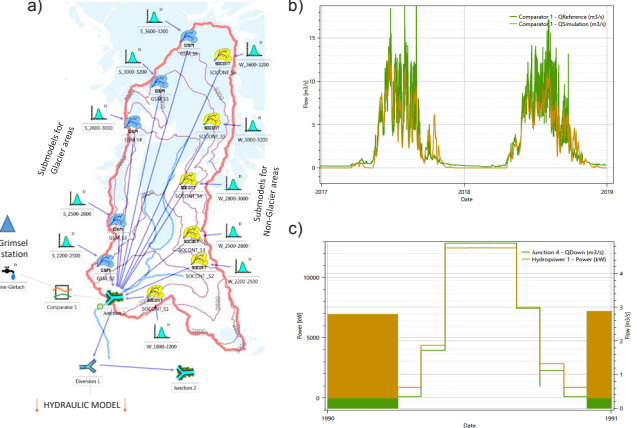

Figure 3: a) Schematic representation of the Gletsch catchment in the RS Minerve sotware, b) Observed and simulated discharge during 2017 and 2018, c) Power production simulated over one year using SSO operation.

Conclusion

- An integrated and numerically efficient hydrology-hydraulic model was developed in order to perform simulations of run-off-river HPP. The calibration of the hydrology model lead to the **accurate simulation** of the observations.

- The construction of a numerical model can easily reproduce different scenarios of energy production allowing for a good prediction of the HPP reaction for a certain inflow while adopting specific operational modes. It is therefore becoming a **relevant operational tool**.

- The **SSO benefit** was highlighted by comparing it with the power production resulted by normal operations. The simulations undertaken along a whole year have shown that the increment in power production during winter season doubles, reaching a gain of more than 700 MWh with respect to the adoption of normal operations.

References

- Farinotti, D. (2013) 'On the effect of short-term climate variability on mountain glaciers: insights from a case study', J. Glaciol., 59(217), pp. 992-1006.
- Gabbi, J., Carenzo, M., Pellicciotti, F., Bauder, A., & Funk, M. (2014). A comparison of empirical and physically based glacier surface melt models for long-term simulations of glacier response. J. Glaciol., 60(224), 1140-1154. doi:10.3189/2014JoG14J011
- Foehn, A., García Hernández, J., Roquier, B., Fluixá-Sanmartín, J. and Paredes Arquiola, J. (2018). Rs minerve – user's manual v2.11. In R. M. Group (Ed.). Switzerland.
- Morand G., Adam N., Manso P, Schleiss A. «« Augmentation de la flexibilité d'exploitation d'aménagements hydroélectriques à haute chute au fil de l'eau en Valais ». SCCER-SoE Science Report 2017.

SCCER-SoE Annual Conference 2019

PyFrac - A planar 3D solver for hydraulic fracture growth

Haseeb Zia, Brice Lecampion

Geo-Energy Laboratory - Gaznat chair on Geo-energy, EPFL, Lausanne, Switzerland

Motivations

Hydraulic fractures are a class of tensile fractures that propagate in response to fluid injection at suffi-cient pressure. At depth in the earth, rocks are under compressive stresses in-situ such that a hydraulic fracture propagates perpendicular to the minimum in-situ stress orientation (minimizing energy) at an in-ection pressure greater than minimum in-situ stress magnitude.

They are used to increase the permeability of porous formation either for enhanced fluid production (geothermal energy, oil and gas production) or storage (CO_2 storage). They are created by engineering fluid injection from deep wellbores. It is a very efficient process allowing to propagate fracture over large distance in a stable manner as the viscous fluid flows into the newly created fracture therefore driving it further as long as injection continues.

Hydraulic fractures also occur naturally in response to local fluid pressurization in the earth crust: for example in association with hydrocarbon generation (diagenesis) but also due to magma pressurization leading to very long vertical buoyant hydraulic fracture eventually reaching the earth surface (leading to so-called lava fissure – see figure 4).

The propagation of fluid-driven fracture exhibits strong non-linearities related to the coupling between mechanical deformation, the creation of new fracture surfaces and the flow of viscous fluid both inside the fracture and in the rock mass (leak-off). The relative balances between i) the energy dissipated in viscous flow versus the one dissipated in fracture creation and ii) the fluid volume stored inside the frac-ture versus the one lost in the rock mass ultimately control propagation. Numerical modeling of such a moving boundary problem is very challenging as it requires the resolution of multiple time and lengths-cales.
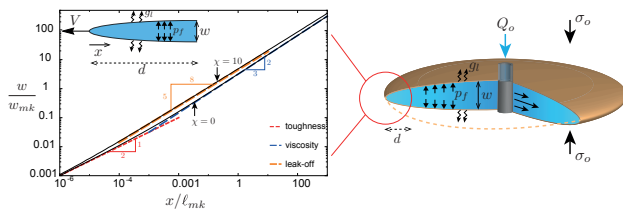
Figure 1: The near-tip behavior of a hydraulic fracture exhibit multiple asymptotic regions related to differ-ent physical processes (left). These asymptotes are valid locally close to the fracture front of a finite hydraulic fracture (right) and can be used to build a robust numerical scheme embedding the multiscale nature of the problem.

Code description

PyFrac is a Python implementation of an implicit level set algorithm originally developed by Peirce & Detournay (2008) to simulate planar Three-dimensional hydraulic fractures. Our implementation makes extensive use of Numpy and Scipy. The numerical scheme has the following features:

- Level set description of the fracture front atop a Cartesian mesh (rectangular elements)
- Multiscale resolution via the coupling of the semi-infinite hydraulic fracture tip solution (see figure 1) with the finite discretization
- Boundary element discretization for quasi-static elasticity
- Finite volume discretization for lubrication flow
- Fully coupled implicit hydro-mechanical solver
- Eikonal equation solved via fast-marching method for fracture front evolution
- Adaptive time-stepping
- Implicit/explicit fracture front advancing
- Remeshing

Current Capabilities

- Isotropic and transversely isotropic elastic infinite medium
- In-homogeneous and anisotropic fracture toughness
- In-homogeneousand leak-off properties
- In-homogeneous in-situ minimum stress
- Buoyant fluid
- Fracture closure and re-opening (multiple injection)
- Time dependent injection history
- Post processing and visualization routines

Verifications

The solver has been validated against all available reference solutions for hydraulic fracture growth. The figures below show the comparison of the solution computed by PyFrac against the semi-analytical solution for a penny shaped hydraulic fracture propagating in the viscosity dominated regime (case of negligible toughness and negligible leak-off).
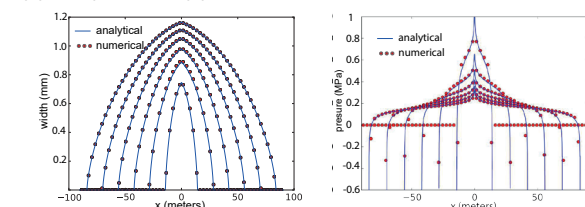

Figure 2: Penny shaped hydraulic fracture viscosity dominated regime benchmark. Fracture width (left) and net pressure (right) profiles at different time evaluated with PyFrac. The results are shown along a slice of the 3D frac-ture made at the x-axis. The semi-analytical solution is also shown for comparison.

References

- Peirce, A., & Detournay, E. (2008). An implicit level set method for modeling hydraulically driven fractures. *Comp. Meth. App. Mech. Engng*, 197(33), 2858-2885.
- Wu, R., Bunger, A. P., Jeffrey, R. G., & Siebrits, E. (2008). A comparison of numerical and experimental results of hydraulic fracture growth into a zone of lower confining stress. In the 42nd US rock mechanics symposium. American Rock Mechanics Association.
- Zia, H., Lecampion, B., & Zhang, W. (2018). Impact of the anisotropy of fracture toughness on the propagation of planar 3D hydraulic fracture. *Int. J. Frac.*, 211(1-2), 103-123.
- H. Zia and B. Lecampion (2019). Explicit versus implicit front advancing schemes for the simulation of hydraulic fracture growth. *Int. J. Numer. Anal. Meth. Geomech.* 43(6):1300–1315.

Validation against a laboratory experiment

We compare numerical predictions against optical measurement of the fracture front obtained in a laboratory experiment performed in a transparent PMMA block (Wu *et al.*, 2008) with three regions of different confining stress (see the figure below for schematics of the experiment). The fluid is injected in the middle layer. Due to the difference in confining stresses, the fracture herniates predominently in the layer having lower stress while being arrested at the boundary of the layer with higher confining stress.
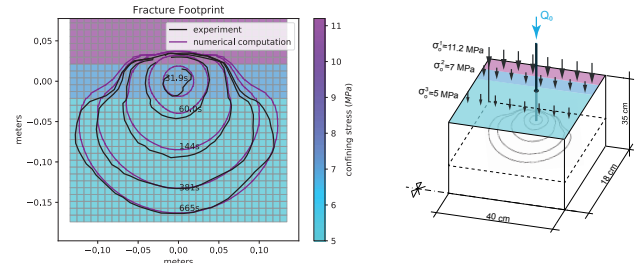

Figure 3: Schematics of the experimental setup showing the PMMA block with three levels of confining stress **(right)**. The fluid is injected in the middle layers and the fracture propagates in a plane at the half depth of the block (shown with a dotted line) perpendicular to the applied confining stresses. Fracture footprint at 31.9, 60, 144, 281 and 665 seconds after the start of injection. The numerical results obtained with PyFrac (magenta lines) compare well with the experimental results (black lines).

Dyke propagation

The buoancy contrast between magma and the surrounding rock drives fracture growth toward the surface. In this illustrative example, we simulate the propagation of a dyke due to a pulse release of magma from a point source at a depth of 6.4km.

Figure 4: Lava fissure appearing on Hawaii's Big Island on May 5, 2018. It corresponds to the emer-gence of a dyke propagating due to magma release from deep chambers (Kilauea volcano).
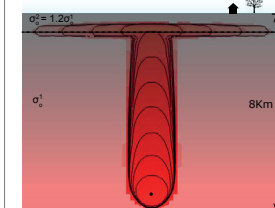
Figure 5: Time evolution of the footprint of the dyke. A pulse of magma is released at the injection point shown by the black dot. As time progresses, the magmatic dyke moves upward until it reaches a layer with 20% larger confining stress (dotted line), causing it to extend laterally.


Figure 6: Fracture width of the dyke at different times. The head and tail structure, typical of buoyan-cy driven fractures can be observed on this 3D plot.

Anisotropy in fracture toughness

We simulate the growth of hydraulic fracture in an anisotropic medium having a higher fracture toughness in the vertical direction as compared to the horizontal direction.

Figure 8: Transition from a radial viscosity dominated hydraulic fracture to an elliptical toughness dominated hydraulic fracture case $K_{I,z}/K_{I,x} = 1.73$. Fracture foot-prints obtained numerically at different times (black lines), with zooms for smaller times from top to bottom. The footprints of the analytical solution for radial viscosi-ty dominated hydraulic fracture are also displayed in red at small times. The local propagation regime along the fracture front is represented by a color code in the cells just behind fracture front, with red being fully viscosity dominated and blue being fully toughness dominated.
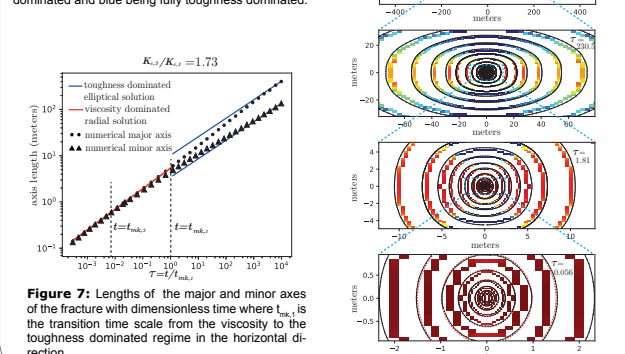
Figure 7: Lengths of the major and minor axes of the fracture with dimensionless time where $t_{mk,x}$ is the transition time scale from the viscosity to the toughness dominated regime in the horizontal di-rection.